Materials Horizons

ROYAL SOCIETY OF CHEMISTRY

COMMUNICATION

View Article Online
View Journal

Published on 30 October 2024. Downloaded by Renmin University of China on 10/30/2024 2:04:31 PM.

Check for updates

Cite this: DOI: 10.1039/d4mh00726c

Received 7th June 2024,
Accepted 21st October 2024

DOI: 10.1039/d4mh00726c

rsc.li/materials-horizons

Twist-angle dependent pseudo-magnetic fields in monolayer $CrCl_2$/graphene heterostructures†

Zhengbo Cheng,‡[a] Nanshu Liu,‡[b] Jinghao Deng,[a] Hui Zhang,[a] Zemin Pan,[a] Chao Zhu,[a] Shuangzan Lu,[ad] Yusong Bai,[a] Xiaoyu Lin,[a] Wei Ji*[b] and Chendong Zhang*[ac]

The generation of pseudo-magnetic fields in strained graphene leads to quantized Landau levels in the absence of an external magnetic field, providing the potential to achieve a zero-magnetic-field analogue of the quantum Hall effect. Here, we report the realization of a pseudo-magnetic field in epitaxial graphene by building a monolayer $CrCl_2$/graphene heterointerface. The $CrCl_2$ crystal structure exhibits spontaneous breaking of three-fold rotational symmetry, yielding an anisotropic displacement field at the interface. Using scanning tunneling spectroscopy, we have discovered a sequence of pseudo-Landau levels associated with massless Dirac fermions. A control experiment performed on the $CrCl_2$/$NbSe_2$ interface confirms the origin as the pseudo-magnetic field in the graphene layer that strongly interacts with $CrCl_2$. More interestingly, the strength of the pseudo-magnetic fields can be tuned by the twist angle between the monolayer $CrCl_2$ and graphene, with a variation of up to threefold, depending on the twist angle of 0° to 30°. This work presents a rare 2D heterojunction for exploring PMF-related physics, such as the valley Hall effect, with the advantage of easy and flexible implementation.

New concepts

Inhomogeneous deformation of graphene has the capacity to generate a pseudomagnetic field (PMF), which gives rise to novel electronic characteristics in the absence of a real external magnetic field. A scalable approach to incorporating PMF in graphene is based on the creation of moiré superlattices; however, this approach is typically constrained to very small twist angles in bilayer graphene. It is anticipated that heterostacking with symmetry-mismatched van der Waals layers will overcome the limitations on twist angles. Nevertheless, the experimental demonstration of a pronounced PMF with a range of twist angle is a rare occurrence. Herein, we report the realization of tunable pseudo-magnetic fields in epitaxial graphene that are not constrained by the twist angle by building a symmetry-breaking monolayer $CrCl_2$/graphene heterostructure. The strength of the PMF can be tuned by the twist angle between the monolayer $CrCl_2$ and graphene; a change in the angle from 0° to 30° can result in a threefold difference in the field strength. This work presents a rare 2D heterostructure for exploring PMF-related physics, with the advantage of easy and flexible implementation.

Introduction

The phenomenon of strain-induced pseudo-magnetic field (PMF) in graphene has garnered significant attention in recent years.[1,2] PMF is a form of gauge field that mimics electron behavior in a real magnetic field, revealing the characteristics of Landau quantization.[3] Unlike the real magnetic fields, the pseudo-magnetic field maintains the time-reversal symmetry and has opposite signs at the two K valleys, resulting in a valley Hall effect.[4,5] It has been theoretically understood that non-uniform shear strain is the key factor producing finite PMF, while uniaxial or isotropic strain has zero net field.[2,6] The experimental realization of the PMF (and the corresponding discrete Landau levels) in graphene is primarily achieved through local deformations, either by randomly formed bubbles/ripples[5,7,8] or by artificially fabricated nanostructures.[9–12] A more scalable approach to introducing the PMF lies in the moiré superlattice, which is usually accompanied by out-of-plane corrugation and minor in-plane displacements.[13,14] Although moiré patterns commonly occur when stacking two van der Waals (vdW) layers together, the presence of PMF is mostly limited to bilayer graphene (or graphene/hBN heterostructures) with a small twist angle.[14,15] This is because when the twist angle is small, the relatively intense inter-layer atomic interaction favors deforming the two lattices with strain gradient, while at larger twist angles, the two lattices are more likely

[a] School of Physics and Technology, Wuhan University, Wuhan 430072, China. E-mail: cdzhang@whu.edu.cn
[b] Beijing Key Laboratory of Optoelectronic Functional Materials and Micro-Nano Devices, School of Physics, Renmin University of China, Beijing 100872, China. E-mail: wji@ruc.edu.cn
[c] Wuhan Institute of Quantum Technology, Wuhan, 430206, China
[d] Hubei Jiufengshan Laboratory, Wuhan, 430074, China

† Electronic supplementary information (ESI) available. See DOI: https://doi.org/10.1039/d4mh00726c

‡ These authors contributed equally to this work.

Published on 30 October 2024. Downloaded by Renmin University of China on 10/30/2024 2:04:31 PM.

to act independently.[15] Stacking graphene with vdW layers without C_3 rotational symmetry, *i.e.*, the symmetry mismatch, leads to non-rotationally symmetric interface interactions. This may naturally remove the above limitation on the twist angle. The experimental realization of pronounced PMF with a range of twist angles is rare, except for a pioneering work on graphene/black phosphorous.[13] However, the puckered honeycomb structure of black phosphorus necessitates the use of thicker layers, which limits its applications. Therefore, it is essential to explore a more rigid single-layer material that lacks C_3 rotational symmetry.

Here, we report on a new platform to realize PMF in a symmetry-mismatched heterostructure, *i.e.*, monolayer $CrCl_2$ on top of epitaxial graphene, with the twist angle being tunable from 0° to 30°. While the bulk crystal of $CrCl_2$ has been synthesized before, its thin-film layers, not to mention the monolayer limit, have never been achieved so far. We adopt molecular beam epitaxy (MBE) to successfully synthesise monolayer $CrCl_2$ through the decomposition of a pre-formed $CrCl_3$ monolayer. By using scanning tunneling microscopy/spectroscopy (STM/S), we found that monolayer $CrCl_2$ is a wide gap semiconductor. Intriguingly, a cascade of peaks was observed near the Dirac point of graphene, whose energy levels can be well depicted by the Landau levels of massless Dirac fermions, indicating the appearance of a pseudo-magnetic field. In addition, we have demonstrated that the intensity of PMF exhibits a monotone decreasing by a factor of 3 as the twist angle in $CrCl_2$/graphene heterostructures varies from 0° to 30°. Our maximum twist angle exceeds that of the graphene/black phosphorus work (12.4°), enabling a broader adjustment range. Our work provides a promising approach to introduce twistable moiré induced PMF in the epitaxially grown graphene that offers significant advances in the sample quality and size compared to the cleave-transferring graphene used in the graphene/black phosphorus studies.[16]

Results and discussion

In our experiments, the $CrCl_3$ monolayer was first grown on epitaxial graphene/SiC(0001) following a previously reported procedure.[17] It is known that under moderate thermal heating, $CrCl_3$ can decompose into $CrCl_2$.[18,19] However, direct synthesis of monolayer $CrCl_2$ through this decomposition is impeded by the desorption of $CrCl_3$ from the graphene surface at a slightly lower temperature. As shown in Fig. S1 (ESI†), this difficulty was overcome by a small amount of $NbSe_2$ deposition, which creates $CrCl_3$–$NbSe_2$ lateral heterojunctions that inhibit the desorption at the subsequent decomposition reaction. The comparison of the structures of $CrCl_3$ before annealing and $CrCl_2$ after annealing is presented in Fig. S2 (ESI†). Fig. 1a presents a typical STM topographic image of the as-grown sample, showing that the monolayer $CrCl_2$ flake is always formed adjacent to monolayer $NbSe_2$.

Fig. 1b is an atomically resolved image of the monolayer $CrCl_2$. Note that previous studies have suggested that the $CrCl_2$ monolayer is expected to exhibit 1-T crystal structure with C_{3v} symmetry.[20] Though top-layer Cl atoms appear to form a hexagonal lattice, direct measurements of the lattice constants along three supposedly "equivalent" directions are not equal, *i.e.*, $a_2 = a_3 > a_1$, as shown in Fig. S3 (ESI†). A more evident result lies in the fast Fourier transformation (FFT) analysis of an atomically resolved image, as displayed in Fig. 1d. The Bragg peaks q_1, q_2 and q_3, marked in yellow, green and red, respectively, appear as rather sharp spots indicating their uniform

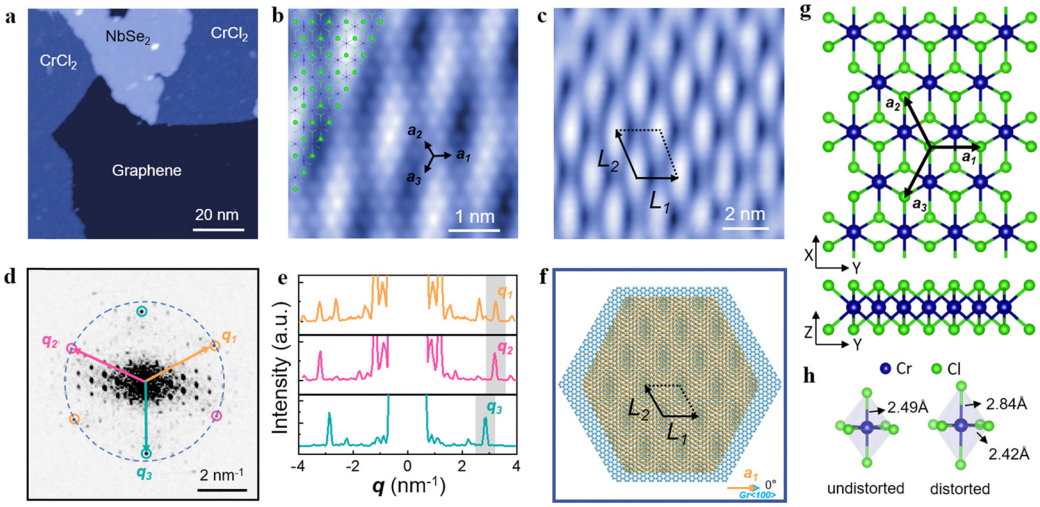

Fig. 1 Morphology and atomic structures of monolayer $CrCl_2$. (a) STM topographic image of $CrCl_2$ film (V_{Bias} = 1.5 V, I_t = 3 pA). (b) Atomically resolved images of the monolayer $CrCl_2$ with an overlaid schematic model (V_{Bias} = 0.4 V, I_t = 10 pA). (c) STM images of the monolayer $CrCl_2$ (V_{Bias} = 1.5 V, I_t = 10 pA). (d) The FFT image of an atomically resolved image. (e) Line profiles along q_1, q_2 and q_3 in (d). (f) The schematic models showing moiré patterns at θ = 0°. (g) Top and side views of the atomic structural model of a $CrCl_2$ monolayer. (h) The schematic diagram of $CrCl_6$ octahedra. Blue and green balls represent Cr and Cl atoms, respectively.

 This journal is © The Royal Society of Chemistry 2024

Published on 30 October 2024. Downloaded by Renmin University of China on 10/30/2024 2:04:31 PM.

distribution over the sample (Fig. 1d). Furthermore, they display varying lengths, with q_3 being less than q_1 and q_2. The exact numbers of reciprocal vectors drawn from Fig. 1e give the lattice constants a_1 = 0.348, a_2 = 0.391, and a_3 = 0.393 nm. The detailed calibrations to eliminate slightly anisotropic responses of the piezo scanner and the derivation processes of a from q are shown in Fig. S4 (ESI†). Our first-principle calculations also reproduce the distortion of the $CrCl_2$ crystal structure. The relaxed structure (Fig. 1g and h) shows that the $CrCl_6$ octahedra got elongated along one of the Cr–Cl bonding directions, resulting in Cr–Cl bond lengths of 0.284 nm and 0.242 nm (compared to 0.249 nm before relaxation[20]). The theoretical values of a_1, a_2 and a_3 are 0.349 nm, 0.389 nm, and 0.391 nm, respectively, which are in good agreement with the experimental observations. Our finding of the C_3 rotational symmetry breaking in monolayer $CrCl_2$ resembles recent reports for CrI_2 and $CrBr_2$.[21,22]

Furthermore, one can observe the formation of a moiré superlattice between the $CrCl_2$ and graphene (as shown in Fig. 1c). The identification of the moiré pattern can be found later. This moiré pattern deviates significantly from the hexagonal lattice, with a parallelogram unit cell measuring L_1 = 1.90 nm and L_2 = 2.02 nm. With the above identified distortions in the $CrCl_2$ structure, we are able to acquire an accurate simulation of the observed parallelogram superstructure (Fig. 1f). Here, the twist angle θ between $CrCl_2$ and graphene, defined by the a_1 of $CrCl_2$ and graphene ⟨100⟩ (Fig. 1f), is 0° as determined by direct measurements of the atomic lattices of $CrCl_2$ and the nearby exposed graphene.

In our experiments, we found that the $CrCl_2$ layer has no preferred orientation with respect to the graphene substrate. A series of twist angle dependent moiré patterns can be found on the surface of the $CrCl_2$ monolayer. Fig. 2a–d shows a set of images with typical θ values of 6°, 9°, 19° and 30°, respectively, while the corresponding simulations are displayed in Fig. 2e–h. The super-periodicities, exemplified by L_2, decrease monotonously with the increase of the twist angle, which is 1.02 nm, 0.83 nm and 0.62 nm for 6°, 9° and 19°. At θ = 30°, the moiré patterns become almost imperceptible in both experiments and simulations. It is worth noting that the tunable moiré features were absent in previous studies of chromium dihalide/graphene systems.[21] In our case, as shown in Fig. S5 and S6 (ESI†), pre-grown $NbSe_2$ provides the attractive possibility of studying the moiré physics in chromium dihalide-graphene heterostructures.

The electronic properties of the $CrCl_2$/graphene heterostructure are characterized through dI/dV spectroscopic measurements. The dI/dV conductance is related to the local density of states of the sample under the STM tip. The dI/dV spectra acquired from the $CrCl_2$/graphene heterostructure demonstrate that the occupied and unoccupied states start at −1.85 and 1.85 eV, respectively, with a resulting band gap of approximately 3.7 eV, indicating $CrCl_2$ as a wide bandgap semiconductor (Fig. 3a). The Fermi level is found to be situated in the middle of the band gap, suggesting that the monolayer $CrCl_2$ on graphene exhibits negligible charge transfer.

Furthermore, the density of electronic states of graphene beneath the $CrCl_2$ layer was directly assessed using dI/dV spectroscopy. To investigate the electron density of states of graphene beneath $CrCl_2$, it was necessary to further decrease the tip–sample distance.[23–25] By utilizing a set point of V_{Bias} = −0.1 V and I_t = 100 pA, the density of states of the underlying graphene close to the Fermi level is determined. Notably, the dI/dV curve near the Fermi level of the $CrCl_2$/graphene heterostructure exhibited a series of peaks, as shown in Fig. 3b. These conductance peaks resemble those observed in previous STM measurements of graphene heterostructures, where the strain-induced pseudo-magnetic field leads to the formation of pseudo-Landau levels (pLLs).[13] Graphene can be subjected to strain textures when combined with materials having lattice

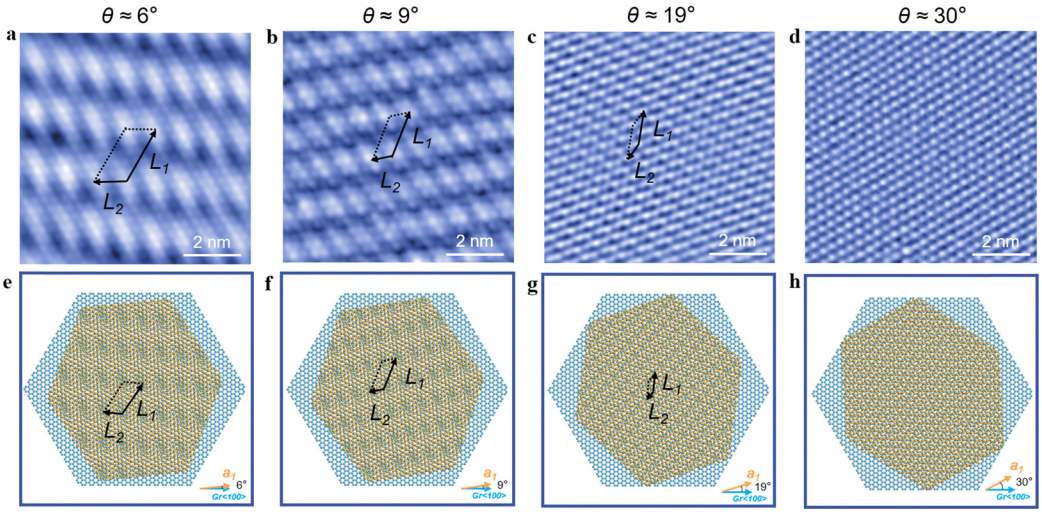

Fig. 2 θ-Dependent moiré superlattices of $CrCl_2$–graphene heterostructures. (a)–(d) STM topography images show the evolution of moiré superlattices of $CrCl_2$ on an epitaxial graphene/SiC(0001) substrate (V_{Bias} = 0.4 V, I_t = 10 pA). (e)–(h) Moiré patterns are simulated with twist angles identical to those of (a)–(d), respectively.

Published on 30 October 2024. Downloaded by Renmin University of China on 10/30/2024 2:04:31 PM.

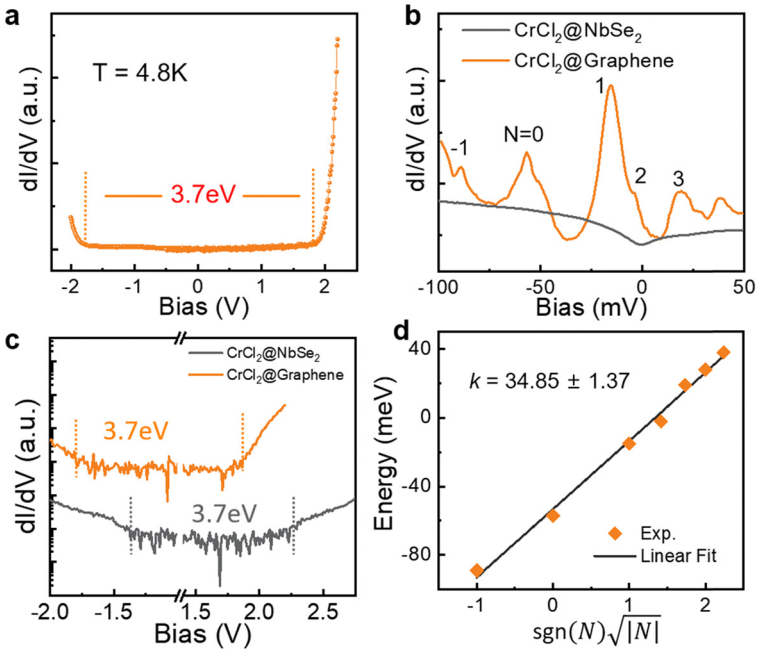

Fig. 3 Electronic structures and pseudo-Landau levels in $CrCl_2$–graphene heterostructures. (a) d*I*/d*V* curve taken on a $CrCl_2$ surface revealing its typical semiconducting nature (V_{Bias} = 2.2 V, I_t = 30 pA). (b) d*I*/d*V* spectra of $CrCl_2$ around the Fermi level on the graphene (orange) and $NbSe_2$ (gray), V_{Bias} = −0.1 V, I_t = 100 pA. Peaks are labeled by their corresponding LL index. (c) d*I*/d*V* curves of $CrCl_2$ on graphene and $NbSe_2$ in logarithmic scale (V_{Bias} = −0.1 V, I_t = 100 pA), respectively. (d) The linear fit of peak energy *versus* square-root of LL index N.

mismatches, particularly non-hexagonal materials with differing symmetries.[13] In the absence of an external magnetic field, pseudo-Landau levels can also be induced in strained epitaxial graphene.[9] Consequently, the observed conductance peaks are likely attributed to quantized pLLs arising from the strain-induced pseudo-magnetic field. The energies of these quantized pLLs follow the equation:[26]

$$E_N = E_D + \mathrm{sgn}(N)\nu_F\sqrt{2e\hbar|N|B_S} \quad (1)$$

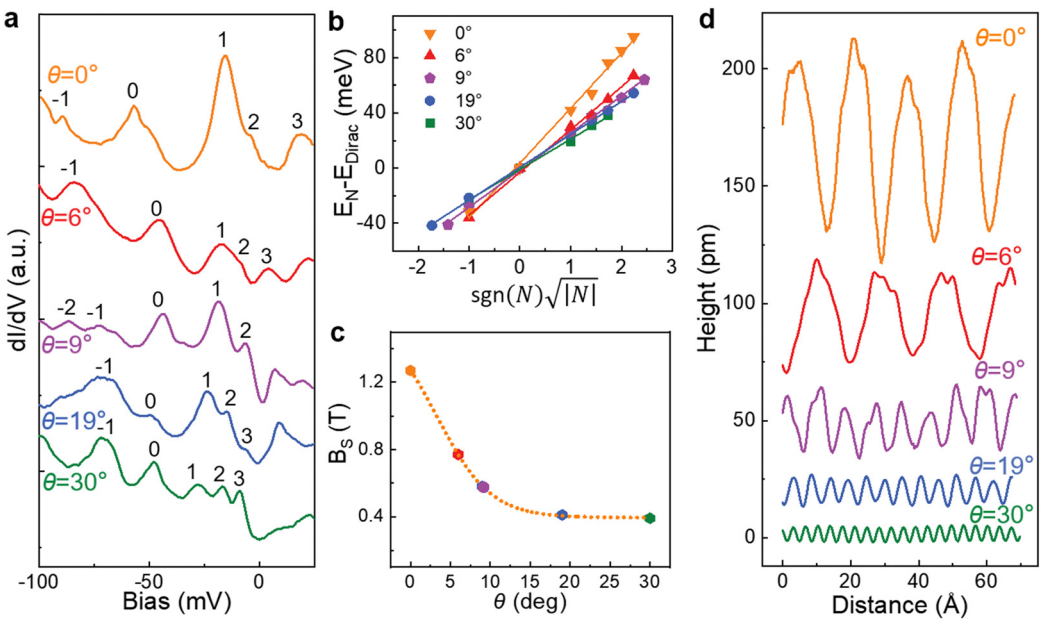

Fig. 4 Twist angle dependent pseudo-magnetic fields. (a) d*I*/d*V* spectra of $CrCl_2$ on the substrate of graphene with $\theta \approx 0°$, 6°, 9°, 19° and 30°. Peaks are labeled by their corresponding LL index (V_{Bias} = −0.1 V, I_t = 100 pA). (b) The linear fit of normalized peak energy *versus* square-root of LL index *N*. $\theta \approx 0°$, 6°, 9° 19° and 30° are plotted with different colors as labeled. (c) Measured pseudo-magnetic field as a function of twist angle in the $CrCl_2$–graphene system. The orange guideline shows the observed trend. (d) Line profiles of $CrCl_2$ with different twist angles showing the buckling of superlattices along the L_2 measured by STM.

 This journal is © The Royal Society of Chemistry 2024

Published on 30 October 2024. Downloaded by Renmin University of China on 10/30/2024 2:04:31 PM.

Here, E_N and E_D are the energy of the Nth Landau level and the energy of the Dirac point, $\hbar$ is the reduced Planck constant, e is the electron charge, v_F is the Fermi velocity, and B_s is the magnitude of the pseudo-magnetic field. In Fig. 3b, the locations of pLLs peaks are labeled by LL index N. The linear relationship between the peak energy and $\mathrm{sgn}(N)\sqrt{|N|}$, as depicted in Fig. 3d, aligns with the scaling behavior as outlined in eqn (1). This correspondence suggests that the conductance peaks arise from pLLs. By fitting the experimental data to eqn (1) and considering the Fermi velocity of graphene as $v_F = 1.0 \times 10^6$ m s^{-1},[27–29] an estimation of $B_S \sim 1.27$ T is derived.

To rule out the possibility of in-gap states of $CrCl_2$ resulting from its lattice distortion or moiré potential, we fabricated a vertical heterojunction of $CrCl_2/NbSe_2$, using $NbSe_2$ as a substrate (Fig. S7, ESI†). The band gap size and atomic structure of $CrCl_2$ in this vertical heterojunction are essentially identical to those observed on graphene (Fig. 3c and Fig. S8, ESI†). Within the $CrCl_2$ band gap, only the electronic states of monolayer $NbSe_2$ can be probed throughout the on-top insulating layer, and no series of peaks are observed (Fig. 3b and Fig. S9, ESI†), which excludes the conduction peaks originating from $CrCl_2$. Additionally, the moiré periodic potential alters the local density of states within the graphene layer, potentially leading to the emergence of distinct peaks in the STS spectra.[15,30] However, it is noted that the relationship between the energy of these peaks and the index N follows $E_N \propto N$ rather than $\sqrt{N}$.[31]

Next, we explores the twist angle dependence of the pseudo-magnetic fields. The representative dI/dV spectra of five superlattices with twist angles of approximately 0°, 6°, 9°, 19° and 30° are depicted in Fig. 4a. These spectra exhibit a series of distinct peaks with varying pLLs spacings. In Fig. 4b, the relationship between the normalized energy $E_N - E_D$ and the $\mathrm{sgn}(N)\sqrt{|N|}$ of the five superlattices is depicted. According to the fitting of each dataset with eqn (1), the PMFs are calculated to be approximately 1.27, 0.77, 0.58, 0.41 and 0.39 T for twist angles of around 0°, 6°, 9°, 19° and 30°, respectively. It is observed that the PMFs consistently decrease with an increase in the twist angle, as illustrated in Fig. 4c. In Note S1 (ESI†), we show that the Landau level spacing is affected by the twist angle. Furthermore, Fig. 4d illustrates the comparison of the buckling behavior of five superlattices at twist angles of 0°, 6°, 9°, 19° and 30°. A noticeable trend of out-of-plane buckling (denoted as h) is observed through the measurement of the apparent height along the L_2 direction: $h_{0°} > h_{6°} > h_{9°} > h_{19°} > h_{30°}$. This trend suggests that the out-of-plane deformations diminish gradually as the twist angle increases. In the vdW heterostructure, the inter-layer forces are influenced by both the twist angle θ and lattice mismatch δ. These forces induce strains in both layers, which are partially relieved by deformation occurring out of the plane.[32] Consequently, the measurement of out-of-plane deformation may serve as an indicator of the magnitude of graphene strain. As the twist angle increases incrementally, the out-of-plane deformation is observed to decrease gradually, signifying a gradual reduction in strain, which aligns with the experimental findings.

Conclusion

In summary, $CrCl_2$ films down to the single-layer limit are prepared on an epitaxial graphene surface with the assistance of lateral bonding (with $NbSe_2$ in our case). The twist angles between $CrCl_2$ and graphene can be adjusted to produce various moiré patterns, as our findings suggest. STS measurements revealed a sequence of pLL peaks in the DOS consistent with the strain-induced PMF. Furthermore, we demonstrate that the strength of PMF can be adjusted by the rotation angle of $CrCl_2$ on the graphene. The 2D van der Waals heterostructures composed of magnetic semiconductors and graphene provide a platform for future studies on low-dimensional magnetoelectric phenomena, while also offering the potential for achieving a high-quality, large-scale, and well-established platform for pseudo-magnetic fields. In addition, a single fabrication affording the possibility of neighboring lateral heterojunctions (*i.e.*, the $CrCl_2/NbSe_2$), promotes single device architectures with different physics in neighboring heterojunctions.

Methods

Preparation of the $CrCl_2$/graphene heterostructures

The heterostructures were fabricated within a molecular beam epitaxy (MBE) chamber that maintained a base pressure better than 2×10^{-10} torr. Before growth, an epitaxial graphene substrate was prepared by silicon sublimation from the 6H-SiC(0001) wafer. High-purity separated Nb (99.5%) and Se (99.999%) sources were evaporated from an electron-beam evaporator and a homemade Knudsen cell, respectively. The flux ratio of Nb/Se was estimated to be 1 : 20. The pre-grown $NbSe_2$ inhibited desorption in the subsequent decomposition reaction. An anhydrous powder of $CrCl_3$ (99%) was evaporated from a homemade Knudsen cell. The rate of growth, approximately 0.02 monolayer per min, was ascertained by monitoring the coverages of the samples. The substrate was kept at 520 K during growth. The $CrCl_2$ samples were obtained through subsequent vacuum annealing at 580 K for 0.5 h, which results in the decomposition of $CrCl_3$ and the formation of $CrCl_2$. After growth, the sample was then transferred from the MBE chamber to the STM chamber under an ultra-high vacuum environment.

Scanning tunneling microscopy and spectroscopy

The STM/S measurements were conducted using a commercial Unisoku 1300 system at 4.4 K in ultra-high vacuum ($<1 \times 10^{-10}$ torr). An electrochemically etched tungsten tip was cleaned by electron beam bombardment and calibrated on a standard Cu(111) sample before the measurements. The tunneling dI/dV spectra were obtained by using a standard lock-in amplifier with a modulation voltage frequency of 932 Hz while maintaining a constant tip–sample distance.

Published on 30 October 2024. Downloaded by Renmin University of China on 10/30/2024 2:04:31 PM.

Data availability

The data that support the findings of this study are available from the corresponding author upon reasonable request.

Author contributions

Z. C. B., N. S. L., W. J., and C. D. Z. conceived the idea and designed the study. Z. C. B. carried out the MBE growth and STM/S measurements with assistance from C. D. Z. N. S. L. and W. J. performed the first-principles calculations. J. H. D., H. Z., Z. M. P., C. Z., S. Z. L., Y. S. B., and X. Y. L. participated in the experiments and analyzed data. Z. C. B., N. S. L., W. J., and C. D. Z. wrote the manuscript and all authors commented on it.

Conflicts of interest

There are no conflicts to declare.

Acknowledgements

The authors gratefully acknowledge the National Natural Science Foundation of China (Grant No. 12134011). W. J. gratefully acknowledges financial support from the Fundamental Research Funds for the Central Universities, and the Research Funds of Renmin University of China (Grant No. 22XNKJ30). N. L. was supported by the China Postdoctoral Science Foundation (2022M713447).

References

1 F. de Juan, J. L. Mañes and M. A. H. Vozmediano, *Phys. Rev. B: Condens. Matter Mater. Phys.*, 2013, **87**, 165131.
2 M. A. H. Vozmediano, M. I. Katsnelson and F. Guinea, *Phys. Rep.*, 2010, **496**, 109–148.
3 C.-C. Hsu, M. L. Teague, J.-Q. Wang and N.-C. Yeh, *Sci. Adv.*, 2020, **6**, eaat9488.
4 D. Xiao, W. Yao and Q. Niu, *Phys. Rev. Lett.*, 2007, **99**, 236809.
5 S.-Y. Li, Y. Su, Y.-N. Ren and L. He, *Phys. Rev. Lett.*, 2020, **124**, 106802.
6 H. Zhou, N. Auerbach, M. Uzan, Y. Zhou, N. Banu, W. Zhi, M. E. Huber, K. Watanabe, T. Taniguchi, Y. Myasoedov, B. Yan and E. Zeldov, *Nature*, 2023, **624**, 275–281.
7 N. Levy, S. A. Burke, K. L. Meaker, M. Panlasigui, A. Zettl, F. Guinea, A. H. C. Neto and M. F. Crommie, *Science*, 2010, **329**, 544–547.
8 R. Banerjee, V.-H. Nguyen, T. Granzier-Nakajima, L. Pabbi, A. Lherbier, A. R. Binion, J.-C. Charlier, M. Terrones and E. W. Hudson, *Nano Lett.*, 2020, **20**, 3113–3121.
9 P. Nigge, A. C. Qu, É. Lantagne-Hurtubise, E. Mårsell, S. Link, G. Tom, M. Zonno, M. Michiardi, M. Schneider, S. Zhdanovich, G. Levy, U. Starke, C. Gutiérrez, D. Bonn, S. A. Burke, M. Franz and A. Damascelli, *Sci. Adv.*, 2019, **5**, eaaw5593.
10 D.-H. Kang, H. Sun, M. Luo, K. Lu, M. Chen, Y. Kim, Y. Jung, X. Gao, S. J. Parluhutan, J. Ge, S. W. Koh, D. Giovanni, T. C. Sum, Q. J. Wang, H. Li and D. Nam, *Nat. Commun.*, 2021, **12**, 5087.
11 Y. Jiang, J. Mao, J. Duan, X. Lai, K. Watanabe, T. Taniguchi and E. Y. Andrei, *Nano Lett.*, 2017, **17**, 2839–2843.
12 C.-C. Hsu, M. L. Teague, J.-Q. Wang and N.-C. Yeh, *Sci. Adv.*, 2020, **6**, eaat9488.
13 Y. Liu, J. N. B. Rodrigues, Y. Z. Luo, L. Li, A. Carvalho, M. Yang, E. Laksono, J. Lu, Y. Bao, H. Xu, S. J. R. Tan, Z. Qiu, C. H. Sow, Y. P. Feng, A. H. C. Neto, S. Adam, J. Lu and K. P. Loh, *Nat. Nanotechnol.*, 2018, **13**, 828–834.
14 H. Shi, Z. Zhan, Z. Qi, K. Huang, E. van Veen, J. A. Silva-Guillen, R. Zhang, P. Li, K. Xie, H. Ji, M. I. Katsnelson, S. Yuan, S. Qin and Z. Zhang, *Nat. Commun.*, 2020, **11**, 371.
15 C. R. Woods, L. Britnell, A. Eckmann, R. S. Ma, J. C. Lu, H. M. Guo, X. Lin, G. L. Yu, Y. Cao, R. V. Gorbachev, A. V. Kretinin, J. Park, L. A. Ponomarenko, M. I. Katsnelson, Y. N. Gornostyrev, K. Watanabe, T. Taniguchi, C. Casiraghi, H.-J. Gao, A. K. Geim and K. S. Novoselov, *Nat. Phys.*, 2014, **10**, 451–456.
16 G. R. Yazdi, T. Iakimov and R. Yakimova, *Crystals*, 2016, **6**, 53.
17 A. Bedoya-Pinto, J.-R. Ji, A. K. Pandeya, P. Gargiani, M. Valvidares, P. Sessi, J. M. Taylor, F. Radu, K. Chang and S. S. P. Parkin, *Science*, 2021, **374**, 616–620.
18 L. Liu, K. Zhai, A. Nie, W. Lv, B. Yang, C. Mu, J. Xiang, F. Wen, Z. Zhao, Z. Zeng, Y. Gong, Y. Tian and Z. Liu, *ACS Appl. Nano Mater.*, 2019, **2**, 1597–1603.
19 D. Mastrippolito, L. Ottaviano, J. Wang, J. Yang, F. Gao, M. Ali, G. D'Olimpio, A. Politano, S. Palleschi, S. Kazim, R. Gunnella, A. D. Cicco, A. Sgarlata, J. Strychalska-Nowak, T. Klimczuk, R. Joseph Cava, L. Lozzi and G. Profeta, *Nanoscale Adv.*, 2021, **3**, 4756–4766.
20 V. V. Kulish and W. Huang, *J. Mater. Chem. C*, 2017, **5**, 8734–8741.
21 L. Peng, J. Zhao, M. Cai, G.-Y. Hua, Z.-Y. Liu, H.-N. Xia, Y. Yuan, W.-H. Zhang, G. Xu, L.-X. Zhao, Z.-W. Zhu, T. Xiang and Y.-S. Fu, *Phys. Rev. Res.*, 2020, **2**, 023264.
22 J. Zhou, L. Shen, M. D. Costa, K. A. Persson, S. P. Ong, P. Huck, Y. Lu, X. Ma, Y. Chen, H. Tang and Y. P. Feng, *Sci. Data*, 2019, **6**, 86.
23 P. Lyu, J. Sødequist, X. Sheng, Z. Qiu, A. Tadich, Q. Li, M. T. Edmonds, M. Zhao, J. Redondo, M. Švec, P. Song, T. Olsen and J. Lu, *ACS Nano*, 2023, **17**, 15441–15448.
24 H. Zhang, M. Holbrook, F. Cheng, H. Nam, M. Liu, C.-R. Pan, D. West, S. Zhang, M.-Y. Chou and C.-K. Shih, *ACS Nano*, 2021, **15**, 2497–2505.
25 J. Martinez-Castro, D. Mauro, Á. Pásztor, I. Gutiérrez-Lezama, A. Scarfato, A. F. Morpurgo and C. Renner, *Nano Lett.*, 2018, **18**, 6696–6702.
26 E. Y. Andrei, G. Li and X. Du, *Rep. Prog. Phys.*, 2012, **75**, 056501.
27 D. L. Miller, K. D. Kubista, G. M. Rutter, M. Ruan, W. A. de Heer, P. N. First and J. A. Stroscio, *Science*, 2009, **324**, 924–927.

 This journal is © The Royal Society of Chemistry 2024

28 G. Li and E. Y. Andrei, *Nat. Phys.*, 2007, **3**, 623–627.
29 L.-J. Yin, S.-Y. Li, J.-B. Qiao, J.-C. Nie and L. He, *Phys. Rev. B: Condens. Matter Mater. Phys.*, 2015, **91**, 115405.
30 G. J. Slotman, M. M. van Wijk, P.-L. Zhao, A. Fasolino, M. I. Katsnelson and S. Yuan, *Phys. Rev. Lett.*, 2015, **115**, 186801.
31 M. Yankowitz, J. Xue, D. Cormode, J. D. Sanchez-Yamagishi, K. Watanabe, T. Taniguchi, P. Jarillo-Herrero, P. Jacquod and B. J. LeRoy, *Nat. Phys.*, 2012, **8**, 382–386.
32 H. Kumar, D. Er, L. Dong, J. Li and V. B. Shenoy, *Sci. Rep.*, 2015, **5**, 10872.

Published on 30 October 2024. Downloaded by Renmin University of China on 10/30/2024 2:04:31 PM.